Geomechanics and Engineering, *Vol. 29, No. 2 (2022) 99-111*
https://doi.org/10.12989/gae.2022.29.2.099

Experimental investigation on bolted rock mass under static-dynamic coupled loading

Pengqi Qiu[1,2a], Jun Wang*[1], Jianguo Ning[1b], Xinshuai Shi[1c] and Shanchao Hu[1d]

[1]*College of energy and mining engineering, Shandong University of Science and Technology, 579 Qianwangang Road, Qingdao, China*
[2]*College of mining engineering, Taiyuan University of Technology, 18 Xinkuangyuan Road, Taiyuan, China*

(Received April 26, 2021, Revised January 20, 2022, Accepted January 25, 2022)

Abstract. Instability of bolted rock mass has been a major hazard in the underground coal mining industry for decades. Developing effective support guidelines requires understanding of complex bolted rock mass failure mechanisms. In this study, the dynamic failure behavior, mechanical behavior, and energy evolution of a laboratory-scale bolted specimens is studied by conducting laboratory static-dynamic coupled loading tests. The results showed that: (1) Under static-dynamic coupled loading, the stress-strain curve of the bolted rock mass has a significant impact velocity (strain rate) correlation, and the stress-strain curve shows rebound characteristics after the peak; (2) There is a critical strain rate in a rock mass under static-dynamic coupled loading, and it decreases exponentially with increasing pre-static load level. Bolting can significantly improve the critical strain rate of a rock mass; (3) Compared with a no-bolt rock mass, the dissipation energy ratio of the bolted rock mass decreases exponentially with increasing pre-static load level, the ultimate dynamic impact energy and dissipation energy of the bolted rock mass increase significantly, and the increasing index of the ratio of dissipation energy increases linearly with the pre-static load; (4) Based on laboratory testing and on-site microseismic and stress monitoring, a design method is proposed for a roadway bolt support against dynamic load disturbance, which provides guidance for the design of deep underground roadway anchorage supports. The research results provide new ideas for explaining the failure behavior of anchorage supports and adopting reasonable design and construction practices.

Keywords: bolted rock; crack propagation; dissipation energy; dynamic mechanical properties; split Hopkinson pressure bar; static-dynamic coupled loading

1. Introduction

Rockbolts are considered an efficient and economical rock mass reinforcement technique and are widely used in mining and other geotechnical engineering applications, such as slopes, roadways, and powerhouses (Wu *et al.* 2019a). In deep underground mines, bolted rock mass is likely to be subjected to both high static stress and dynamic disturbance (fault slips, strata fractures and collapses, earthquakes, etc.). Under coupled static–dynamic loads, mechanical behaviors of bolted rock mass may be different from that solely under either static or dynamic stress, and its performance is not currently complete understood. Hence, it is critical to study and better understand the failure characterization and mechanism of rock material bolted rock mass.

In recent decades, numerous researchers (Ai *et al.* 2019, Vandermaat *et al.* 2016, Gracaecosta *et al.* 2013, Wu *et al.* 2018, Yu *et al.* 2019, Kozyrev *et al.* 2018, Eremenko *et al.* 2017, Chen *et al.* 2019, Wang *et al.* 2014, Wang *et al.* 2018) have conducted laboratory and field tests complemented by analytical and numerical analyses to investigate the anchorage mechanism of rockbolts. (Chang *et al.* 2017, 2018) studied the failure process and failure modes of a rockbolt anchoring system under dynamic-static coupled loading using experimental investigations. Based on finite element software, bond stress distribution in spatial and temporal expression, bond-slip behaviors and the influences of initial stress state of surrounding rock, initial static load level and anchorage length were evaluated. The failure mechanism was explored, and a bond-slip model was developed. (Wang *et al.* 2018) proposed a new analytical model to describe the axial and shear stress distributions for a fully grouted GFRP (Glass Fiber Reinforced Plastic) rockbolt support system under the joint action of a pre-tension static load and a dynamic blast load. The model can be used to predict the axial stress within the rockbolt and the shear stress at the grout-rock interface for GFRP to help ground support design, performance assessments and blast design to minimize the negative impacts on the ground support system. (Ali and Fatemeh 2013) used FLAC3D software to study the behavior of fully grouted rockbolts under dynamic loading. The results of the analyses

---

*Corresponding author, Ph.D.
E-mail: wangjunsdkjd@126.com
[a]Ph.D.
E-mail: qiupengqi@163.com
[b]Professor
E-mail: njglxh@126.com
[c]Ph.D.
E-mail: xs_shi@cumt.edu.cn
[d]Ph.D.
E-mail: mining2@126.com

http://www.techno-press.org/?journal=gae&subpage=7
ISSN: 2005-307X (Print), 2092-6219 (Online)

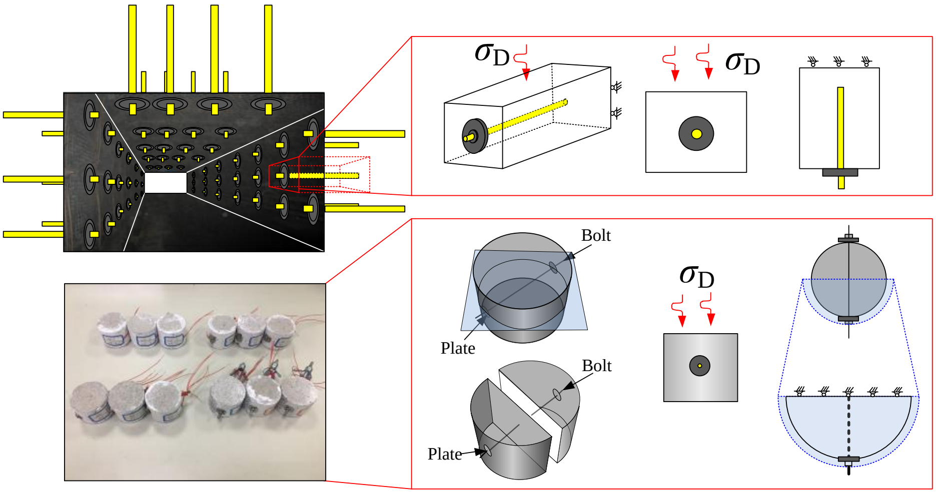

Fig. 1 Rockbolt specimen preparation (σ_S is static loading, σ_D is dynamic loading)

indicated that under dynamic loading, fully grouted rockbolts without a head plate are incapable of controlling rock mass movement. Yielding rockbolts are the best choice for absorbing dynamic stress waves and controlling rock mass movement. (Faham *et al*. 2018) developed numerical and novel analytical simulation techniques for cable bolts to assess their structural behavior under static and dynamic loading conditions. The numerical and analytical models were then validated against experimental observations reported in the literature, which demonstrated the reliability of the proposed models. (Wu *et al*. 2019a, b) conducted static and dynamic Brazilian splitting tests of red sandstone reinforced by a steel bar. The mechanical response characteristics of the rockbolt and the reinforced rock under static and dynamic loadings were investigated extensively, and the results provide a reference for the failure analysis and design of rockbolts. (Freeman 1978) studied the behavior of fully bonded rockbolts in the Kielder experimental tunnel and proposed the concepts of “neutral point”, “anchor length”, and “pick-up length”. Using finite element analysis, (Aydan 2019**)** illustrated the reinforcement effects of bolts on underground openings both qualitatively and quantitatively as well as the interaction phenomena between the bolts and the rock mass. (Fu *et al*. 2019) and (Zhu *et al*. 2018) found that bolts could improve the peak strength, elastic modulus, and shear strength of laboratory specimens. (He *et al*. 2018) and (Sabetamal *et al*. 2014) carried out dynamic tests for a constant resistance large deformation bolt using a modified Split Hopkinson Pressure Bar (SHPB) system. (Kang *et al*. 2020)rock bolt pre-tensioning by torque application to the nut can result in decreases in tensile strength and elongation because the rock bolt is subjected to a combination of tension and distortion. Taking Xinjulong Coal Mine as an example, (Ning *et al*. 2020a, Ning *et al* 2020b) studie the damage evolution characteristics of rock with bolt support in large section chamber under static-dynamic coupling loading by field investigation, theoretical analysis and laboratory test.

The aforementioned studies, conducted under static or dynamic loading conditions, are fundamental and have contributed to a better understanding of the anchorage mechanisms of rockbolts. However, these studies did not consider the influence of field conditions, and they did not consider the combined effects of a static load and a dynamic blast load simultaneously, which is the general loading condition in reality. In this study, static-dynamic coupled loading tests of rockbolt specimens are carried out based on The Split Hopkinson Pressure Bar system. The mechanical properties, energy dissipation and crack growth characteristics of the rockbolt specimens are studied under different loading modes. The results provide a new concept for rational rockbolt design and the construction of deep roadways threatened by static-dynamic coupled loading.

2. Experimental setup

2.1 Specimen preparation

Roof bolting is the primary types to maintain roadway stability by changing the mechanical state of the surrounding rock, forming a whole and stable rock belt around the roadway (Ning *et al*. 2020a). When studying a bolted rock mass formed by a bolt and surrounding rock, the actual boundary conditions of the bolted rock mass should be fully considered. As shown in Fig. 1, the volume of rock under the action of a single bolt is obtained through the average distribution of the volume of surrounding rock under the action of multiple bolts, and the structure formed by the combination of the block and a single bolt is taken as the bolted rock mass unit. The boundary conditions of each bolted rock mass unit are the same. The bolted rock mass unit is constrained by displacement in a direction perpendicular to the bolt.

In this paper, the rockbolt specimens are designed to simulate the actual boundary condition of the bolted rock mass unit. As shown in Fig. 1, the quarter block of the rockbolt specimens is approximately regarded as the bolted rock mass unit, which is composed of a 1/2 bolt and sector column (1/4 rock specimen). According to the principle of symmetry, two vertical planes of a sector are limited by

Table 1 The labels, dimension parameters and loading methods of the specimens

Label	Anchorage type	Pre-static loading (MPa)	Dynamic loading strain rate (/s)				
			First	Second	Third	Fourth	Fifth
D-N-1	No-bolt specimens	0.0	40.6	50.4	62.8	78.1	
D-N-2		1.47	33.6	47.9	63.8		
D-N-3		2.94	37.1	49.9			
D-N-4		4.41	34.8	43.5			
D-N-5		5.88	22.8	38.5			
D-D-1	Rockbolt specimens	0.0	20.9	42.7	67.0	85.6	92.3
D-D-2		1.47	32.4	48.4	65.2	84.0	
D-D-3		2.94	24.1	46.3	60.4	73.0	
D-D-4		4.41	33.8	43.0	54.7	69.2	
D-D-5		5.88	35.1	55.4	66.0		

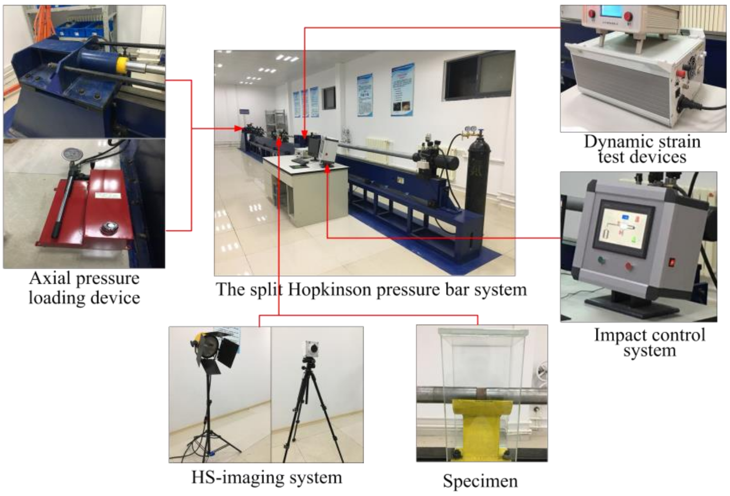

Fig. 2 SHPB dynamic load impact test system

displacement. In this paper, no-bolt specimens are also designed to compare and study the influence of anchor solid elements on the mechanical properties and energy transfer of a rock mass.

Because the uniformity of natural rock mass is poor, sampling is difficult, and conducting laboratory research with similar rock materials instead of original rock specimens is a more reasonable solution. Based on a simulation test method of similar materials, similar rock material specimens were made with cement, sand particles with a size less than 0.56 mm and gypsum. The purpose-built test samples, shown in Fig. 1, were prepared as follows: (1) Cylindrical specimens of 40 mm in thickness and 50 mm in diameter were prepared. These were used for unreinforced tests. For reinforced tests, further preparations were made. (2) Two perpendicular holes with diameters of 5 mm were drilled through the center of the middle circular cross-section of six specimens. (3) Two steel bars were inserted into the hole (simulating the rockbolt) and bonded to the rock with resin. The steel bar was 70 mm long and 4 mm in diameter, with a tensile strength of 500 MPa, a Poisson’s ratio of 0.27 and a Young’s modulus of 200 GPa. (4) All the specimens were polished to a roughness of < 0.02 mm, and the inclination angle between the end circular surfaces and the plane perpendicular to the cylindrical axis was less than 0.001 radians. The labels, dimension parameters and loading methods of the specimens are shown in Table 1.

Ten specimens, listed as of D-N-1~5 and D-D-1~5 in Table 1 were tested under dynamic and static combined loading. The static axial compression was set at 0%, 20%, 40%, 60% and 80% of the peak strength of the no-bolt specimens. Different impact velocities were used to impact the specimens, and the minimum velocity leading to macro cracks was defined as the critical velocity required for the specimen failure of specimens. The dynamic strain test devices were used to record the waveform signals on the incident and transmitted bars during the impact process. At the same time, the whole entire process of cracks growth is being recorded by high-speed camera.

2.2 Experimental system

2.2.1 The split Hopkinson pressure bar system

This experiment was carried out on the split Hopkinsonpressure bar system located at the Key Laboratory of Mine Disaster Prevention and Control, Shandong University of Science and Technology. As shown in Fig. 2, the SHPB test system consisted of five parts: SHPB bars, an axial pressure loading device, an impact control system, dynamic strain test devices and HS-imaging

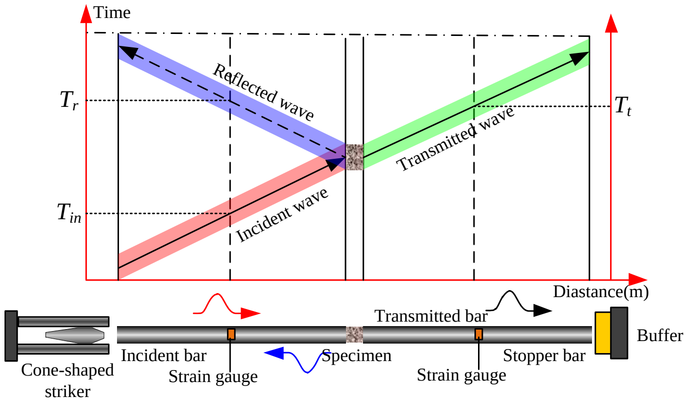

Fig. 3 Schematic diagram of separated Hopkinson pressure bar test system

system. The diameter of the incident, transmission and absorbing bars is 50 mm. The incident and transmission bars were made of 48CrMoA alloy steel with a density of 7850 kg/m^3, a Poisson's ratio of 0.28, and a Young's modulus of 206 GPa. The P wave velocities of the bars were 5120 m/s. The length of the input bars was 3000 mm, and the output bar was 1500 mm. To produce a repeatable ramped pulse wave that reduces high-frequency oscillations (Pochhammer modes) and minimizes the dispersion effect, a cone-shaped striker was used in the present study (The diameter of the striker is 50 mm, the length is 365mm). The input frequency of the strain signal was 1 MHz in the dynamic strain test devices. To capture the images of the specimen during the impact damage process, a Phantom series Vision Research/V410L high-speed camera was used. It can capture the image with a maximum of 600,000 fps and a resolution of 512×272 pixel array size.

2.2.2 Experimental principles

During testing, the specimen was sandwiched between the incident and transmission bars, with lubricant applied to the surfaces of the specimen and bars (Fig. 3). The impact of the cone-shaped striker on the front surface of the incident bar produces a slowly rising half-sine wave. When the compressive wave (incident wave) reaches the bar-specimen interface, a portion is reflected in the incident bar (reflected wave), and another portion is transmitted through the specimen and then enters the transmission bar (transmitted wave). These three elastic stress pulses are recorded by strain gauges mounted on the bars and are denoted as the incident strain pulse ε_i, reflected strain pulse ε_r, and transmitted strain pulse ε_t, respectively. According to the one-wave propagation theory, the axial stress σ_s, strain ε_{sj}, and strain rate $\dot{\varepsilon}_s$ are derived by the following equations

$$\varepsilon_{\mathrm{s}}=\frac{C_0}{l_{\mathrm{s}}}\int_0^{t_0}\left(\varepsilon_{\mathrm{i}}-\varepsilon_{\mathrm{r}}-\varepsilon_{\mathrm{t}}\right)\mathrm{d}t \tag{1}$$

$$\dot{\varepsilon}_{\mathrm{s}}=\frac{C_0}{l_{\mathrm{s}}}\left(\varepsilon_{\mathrm{i}}-\varepsilon_{\mathrm{r}}-\varepsilon_{\mathrm{t}}\right) \tag{2}$$

$$\sigma_{\mathrm{s}}=\frac{EA}{2A_{\mathrm{s}}}\left(\varepsilon_{\mathrm{i}}-\varepsilon_{\mathrm{r}}-\varepsilon_{\mathrm{t}}\right) \tag{3}$$

where A, C_0, and E are the cross-sectional area, P-wave velocity, and Young's modulus of the elastic bar, respectively. A_s and l_s are the cross-sectional area and length of the specimen, respectively.

The dissipated energy (Feng *et al.* 2018) of the no-bolt and rockbolt specimens under dynamic loads can be calculated using the following equation

$$E_{\mathrm{D}}=E_{\mathrm{I}}-\left(E_{\mathrm{R}}+E_{\mathrm{T}}\right) \tag{4}$$

where E_{D} is the dissipated energy of the specimen; E_{I}, E_{R}, and E_{T} are the energy carried by the incident, reflected, and transmitted wave, respectively (Fig. 4), which can be calculated by Eqs. (5)-(7).

$$E_{\mathrm{I}}=A_0\rho_0C_0^3\int_0^t\varepsilon_{\mathrm{I}}^2\left(t_1\right)\mathrm{d}t_1 \tag{5}$$

$$E_{\mathrm{R}}=A_0\rho_0C_0^3\int_0^t\varepsilon_{\mathrm{R}}^2\left(t_1\right)\mathrm{d}t_1 \tag{6}$$

$$E_{\mathrm{T}}=A_0\rho_0C_0^3\int_0^t\varepsilon_{\mathrm{T}}^2\left(t_1\right)\mathrm{d}t_1 \tag{6}$$

where t is the duration of the stress wave; ρ_0 is the density of the bars; C_0 is the elastic wave velocity of the bars; A_0 is the cross-sectional area of the bars; $\varepsilon(t)$ denotes strain in a bar at time t; and the subscripts I, R, and T refer to the incident, reflected, and transmitted wave, respectively.

3. Results

3.1 Stress-strain curves of specimens under Static-dynamic coupleding loading

3.1.1 Stress Equilibrium

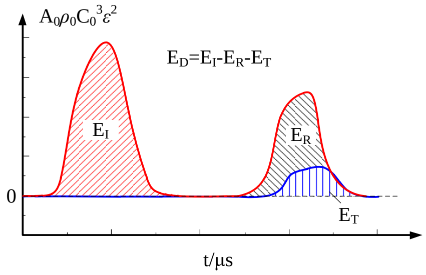

Fig. 4 Energy-time-history curves of incident, reflected and transmitted waves

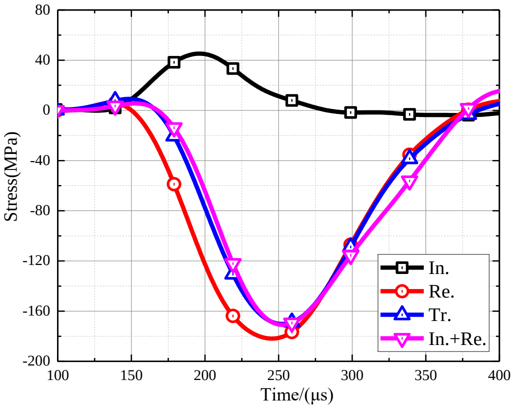

Fig. 5 Dynamic stress on the two interfaces between the specimen and the bars in SHPB testing

Ensuring the homogenization of stress at both ends of the specimen is the key factor for validating the SHPB test (Du *et al*. 2018, Field *et al*. 2004). The results show that the inertia effect is eliminated by means of wave shaping and controlling the length-diameter ratio of the specimen; the stress difference between the two ends of the specimen still exists. With the stress wave reflected back and forth at the end of the incident bar and the transmission bar, the stress distribution in the specimen gradually becomes uniform. At this time, the stress state of the specimen is essentially quasi-static loading. In this work, a cone-shaped striker is used to generate a slowly rising half sine wave with an approximate duration of 200 μs, which provides sufficient time for the specimen to reach stress equilibrium and facilitate loading at a constant strain rate. Fig. 5 shows a comparison of the stresses at both ends of the specimen. The sum of the incident stress and reflected stress is almost equal to the transmitted stress before the transmitted wave reaches its peak value and is well maintained for a certain time in the post-peak region. This result indicates that a stress equilibrium condition can be achieved for the purpose-built test samples in the present SHPB tests.

3.1.2 Stress-strain curves of no-bolt specimens

The dynamic stress–strain curves of no-bolt specimens from different levels under static-dynamic coupled loading are shown in Figs. 6(a)-6(e). As shown in Fig. 6(f), all the dynamic stress–strain curves displayed in Figs. 6(a)-6(e) can be grouped into two general patterns: general pattern one and general pattern two. When the strain rate does not reach the critical strain rate, the stress–strain curves are general pattern one. When the strain rate equals or exceeds the critical strain rate, the stress–strain curves are general pattern two (Peng *et al*. 2019). These two general patterns have three similar stages (stage I, stage II, and stage III). Combined with Fig. 7, the variations in the dynamic stress–strain curves of no-bolt specimens under static-dynamic coupled loading can be elaborated as follows.

Stage I (O-A): The stress-strain curve in stage I does not show a concave shape. The stage is approximately linear and does not show compaction characteristics. It can be seen from the typical crack development process of the no-bolt specimen that there is no crack initiation on the specimen surface at this stage.

Stage II (A-B): During this stage, the stress-strain relationship is nonlinear, and compared with stage I, the growth rate of stress with strain slows down. At point B, crack initiation occurs at both ends of the specimen. At this stage, the microcracks in the specimen begin to develop under the action of dynamic load, resulting in the decrease of the curve slope.

Stage III (B-C): The growth rate of stress with strain is lower than that of stages I and II. The photos show that the macrocracks on the specimen surface develop towards the specimen center under the action of a stress wave. When the curve reaches the peak strength of point C, obvious cracks appear on the surface of the specimen, and the maximum bearing capacity is reached.

Stage IV (C-E): The stress-strain curve of the specimen during this stage shows two modes. One mode indicates that when the striker does not reach the critical speed, due to the low impact strain rate, the rebound occurs after the D point reaches the ultimate strain, and the overall stress-strain curve shows the characteristics of "closure"; the other mode indicates that under the critical impact speed, the macroscopic crack of the specimen expands rapidly,

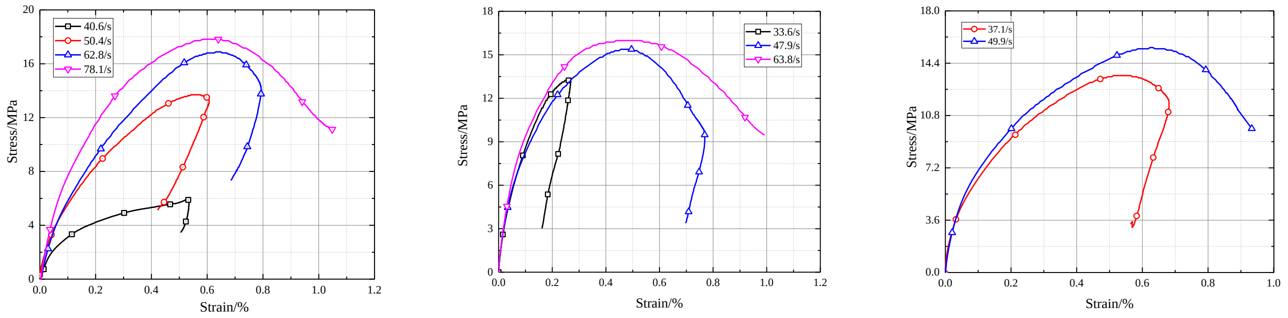

(a) 0 MPa (b) 1.47 MPa (c) 2.94 MPa

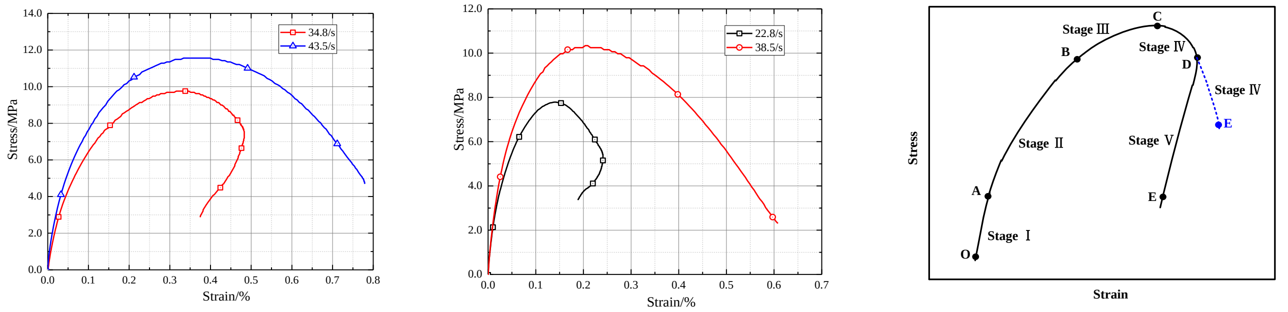

(d) 4.41 MPa (e) 5.88 MPa (f) Typical curves

Fig. 6 Stress-strain curves of no-bolt specimens under static-dynamic coupled loading

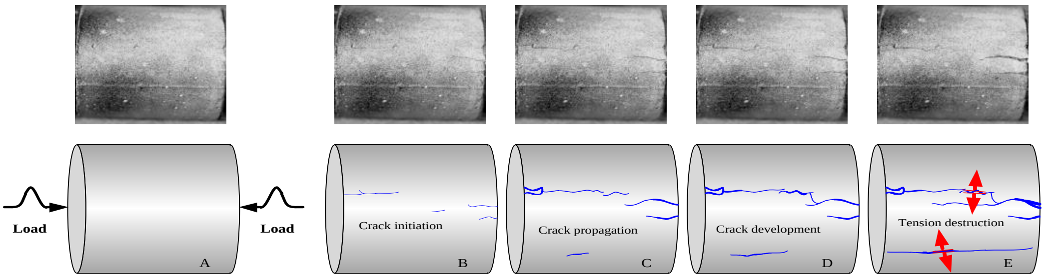

Fig. 7 The typical process of crack development process of no-bolt specimen D-N-1(78.1/s)

resulting in the failure of the specimen. The overall stress-strain curve shows the characteristics of "opening". During the entire failure process, the crack morphology of the specimen primarily consists of tensile cracks.

In addition, the stress-strain curves of the no-bolt specimens described in Fig. 6(a)-6(e) have an impact velocity (strain rate) correlation. Taking the pre-static load of 0 MPa as an example (Fig. 6(a)), the greater the impact velocity is, the greater the peak stress. When the impact strain rate is 40.6/s, 50.4/s and 62.8/s, the peak stresses of the specimens are 6.0 MPa, 13.8 MPa and 16.9 MPa, respectively. After the stress peak, the specimens show a rebound phenomenon and recover part of the strain. When the impact velocity of the striker is 78.1/s, cracks appear in the sample surface, and the peak strength is 17.9 MPa. The stress-strain curve shows the characteristics of "opening". The samples did not exhibit compaction characteristics during different impact loading processes. It can be concluded that under the high strain rate of the specimens during impact loading, the closure time of microvoids is very short, resulting in no compaction phenomenon during the entire loading process. The trend of the stress-strain curves of other specimens under static-dynamic coupled loading Figs. 6(b)-6(e) are similar to the specimen in which the pre-static load is 0 MPa Fig. 6(a). The microcracks in the specimen have been destroyed under pre-static loading, and the compaction phenomenon has completely disappeared. When the pre-static loads of the specimens are 1.47 MPa, 2.94 MPa, 4.41 MPa and 5.88 MPa, the critical strain rates required for no-bolt specimen failure are 63.8/s, 49.9/s, 43.5/s and 38.5/s, and the dynamic strengths of the specimens are 16.1 MPa, 15.3 MPa, 11.6 MPa and 10.3 MPa, respectively. It can be seen that the critical strain rate and dynamic strength required for specimen failure decrease with increasing pre-static load.

3.1.3 Stress-strain curves of the rockbolt specimens

The stress-strain curves of the rockbolt specimens under different static-dynamic coupled loadings are shown in Fig. 8(a)-(e), and Fig. 8(f) shows a typical mode of the rockbolt specimens. Combined with Fig 9, the stress-strain curve of the rockbolt specimen can be divided into four stages according to the crack development characteristics.

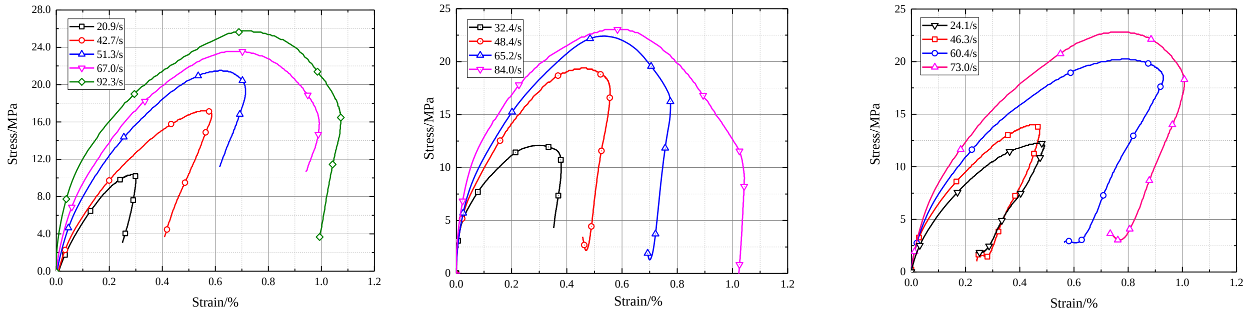

(a) 0 MPa (b) 3.26 MPa (c) 6.52 MPa

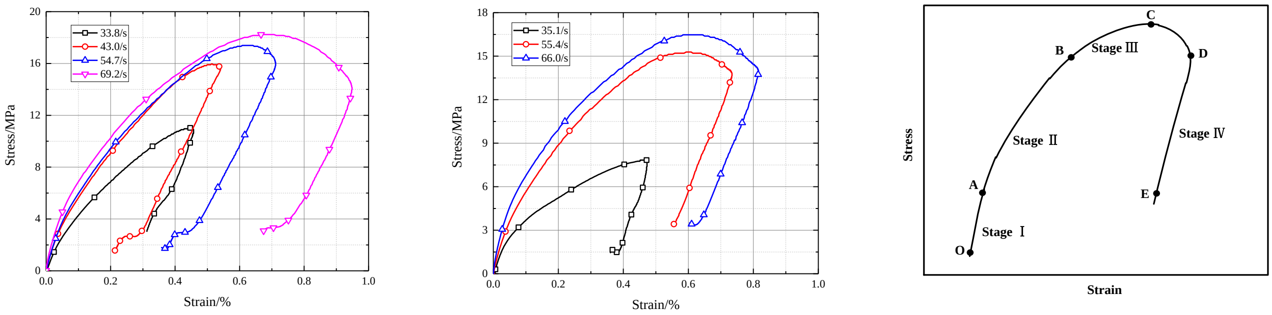

(d) 9.78 MPa (e) 13.04 MPa (f) Typical curves

Fig. 8 Stress-strain curves of rockbolt specimens under static-dynamic coupled loading

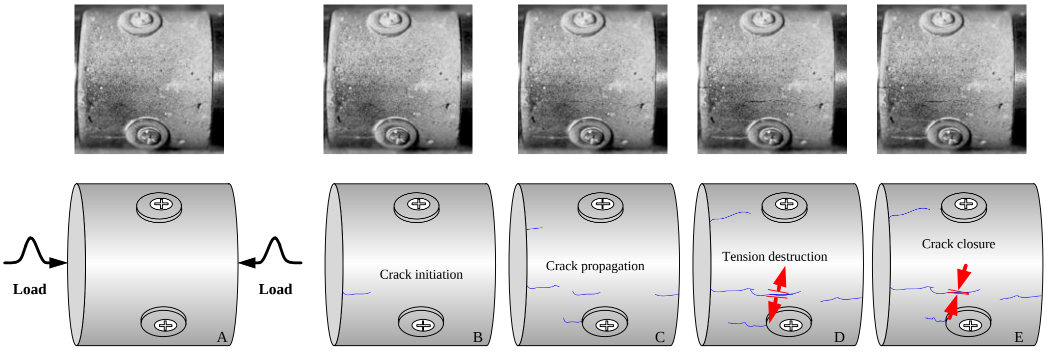

Fig. 9 Typical crack development process of rockbolt specimens

Stage Ⅰ (O-A): This stage is similar to the no-bolt specimen, and the curve does not show concave shape and compaction characteristics. No cracks are apparent on the surface of the no-bolt specimen during this stage.

Stage Ⅱ (A-B): The stress-strain relationship is nonlinear during this stage. Compared with stage Ⅰ, the growth rate of stress with strain slows down. At point B, crack initiation appears on the surface of the specimen. During this stage, the microcracks in the specimen begin to develop under the action of dynamic load, resulting in a decrease of the curve slope.

Stage Ⅲ (B-C): The growth rate of stress with strain is lower than those of the first two stages. The photos show that there are macrocracks at the rockbolt section of the specimen surface under the action of a stress wave. When the curve reaches the peak strength of point C, the specimen reaches the maximum bearing capacity.

Stage Ⅳ (C-E): The stress-strain curves of the rockbolt specimen during this stage only shows one mode compared with that of the no-bolt specimen. After the surface of the rockbolt specimen produces cracks, the stress-strain curve still rebounds after the D point reaches the limit strain, and the overall stress-strain curve shows the characteristics of "closure". Combined with the development characteristics of the surface crack, it can be seen that when the crack develops to point E, it does not continue to extend, but the crack tip is closed. The analysis shows that in the later stage of dynamic impact, the strain rate of the dynamic load decreases, and the bolt, which is in a passive state of elastic tension due to the radial deformation of the specimen, begins to recover its original length, which restrains the continuous development of the internal cracks. The rockbolt specimen recovers the partial deformation, and the surface cracks of the specimen close, which leads to the occurrence of a stress-strain curve rebound under the premise of failure.

It can be seen from the stress-strain curves of the rockbolt specimens under different static-dynamic coupling loadings that when the pre-static load is 0 MPa, the stress-strain curves of the rockbolt specimens also have significant strain rate correlations, and the rebound phenomenon of the

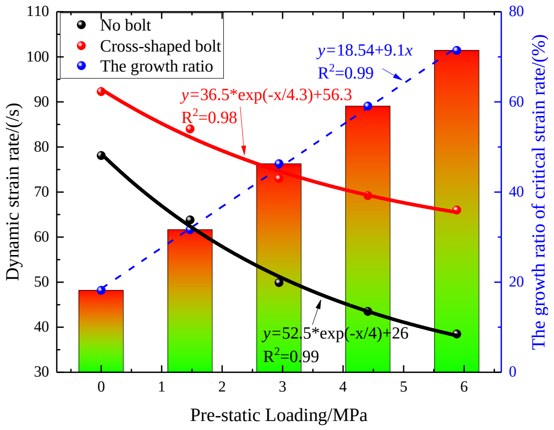

Fig. 10 Critical strain rate of two types of specimens under different pre-static load levels

specimens is extremely obvious. When the impact strain rates are 20.9/s, 42.7/s, 51.3/s and 67.0/s, the samples are not damaged, and the peak stresses are 10.5 MPa, 17.3 MPa, 22.6 MPa and 23.8 MPa, respectively. When the impact strain rate is 92.3/s, there are obvious cracks in the specimen, and the ultimate strength is 25.8 MPa. After the peak of the stress-strain curve, a rebound phenomenon remains, which reflects the action of the rockbolt on the specimen. The trend of the stress-strain curve under static-dynamic coupled loading Figs. 8(b)-8(e) is very similar to Fig. 8(a). The critical strain rate and strength required for the failure of the rockbolt specimen decrease with increasing pre-static loading. When the pre-static loadings are 1.47 MPa, 2.94 MPa, 4.41 MPa and 5.88 MPa, the peak strengths of failure are 23.1 MPa, 22.8 MPa, 18.2 MPa and 16.5 MPa, respectively.

3.2 The critical strain rate of bolted rock mass

Fig. 10 is critical strain rate of two types specimens under different pre-static load levels. It can be seen that there is a critical strain rate in different pre-static loads with increasing dynamic impact velocity. When the impact strain rate of the specimen is lower than the critical strain rate, the specimen is not damaged, and when the impact strain rate is higher than the critical strain rate, the specimen is unstable. The critical strain rate of the specimen under static and dynamic loading is significantly affected by the initial static loading level, and the value decreases exponentially with increasing pre-static load. After bolting, the critical strain rate of the rock specimen is significantly increased, and the critical strain rate is positively related to the pre-static load level. This means that the ability to resist the dynamic load disturbance of a bolted rock mass affected by high static load is significantly improved. By fitting the critical strain rate under different pre-static load levels, the relationship between the two is obtained as follows

$$\dot{\varepsilon}_{\max-N} = 52.5e^{-\frac{P}{4}} + 26 \quad \mathrm{R}^2 = 0.99 \tag{8}$$

$$\dot{\varepsilon}_{\max-C} = 36.5e^{-\frac{P}{4.3}} + 56.3 \quad \mathrm{R}^2 = 0.98 \tag{9}$$

where $\dot{\varepsilon}_{\max-N}$ is the critical strain rate of the no-bolt specimen; $\dot{\varepsilon}_{\max-C}$ is the critical strain rate of the rockbolt specimen; and P is the pre-static loading.

To quantify the effect of the rockbolt on the critical strain rate, a critical strain rate increase ratio is proposed for the rockbolt specimen. Under static-dynamic coupled loading, the critical strain rate increase ratio of the rockbolt specimen is as follows

$$\phi = \frac{\dot{\varepsilon}_{\max-C} - \dot{\varepsilon}_{\max-N}}{\dot{\varepsilon}_{\max-N}} \tag{10}$$

Where ϕ is the critical strain rate increase ratio;

The relationship between the critical strain rate increase ratio and the pre-static load is as follows

$$\phi = 9.1P + 18.54 \tag{11}$$

3.3 Improvement of rock dynamic mechanical properties by bolt

Compression deformation is an important mechanical property of rock. The strength and ultimate strain of the specimen are measured when it is damaged. The quantitative relationship between the dynamic mechanical parameters and the pre-static load is obtained by fitting the data points. It can be seen from (Figs. 11(a) and 11(b)) that the strength of the two types of specimens decreases linearly with the increase of the pre-static load level, and the ultimate strain of the two types of specimens decreases exponentially with the increase of the pre-static load level. The strength and ultimate strain of the rockbolt specimens under the same pre-static load level are significantly higher than those of the no-bolt specimen. The analysis shows that the larger the pre-static load is, the more fully the micropores are closed and the larger the axial strain is before the dynamic load, which results in a decrease in the ultimate strain and strength with the pre-static load level. Due to the lateral restraint of the rockbolt to the specimen, the radial expansion of the specimen is limited, and the axial load that the specimen can bear is increased. This is the reason that the strength and ultimate strain of the

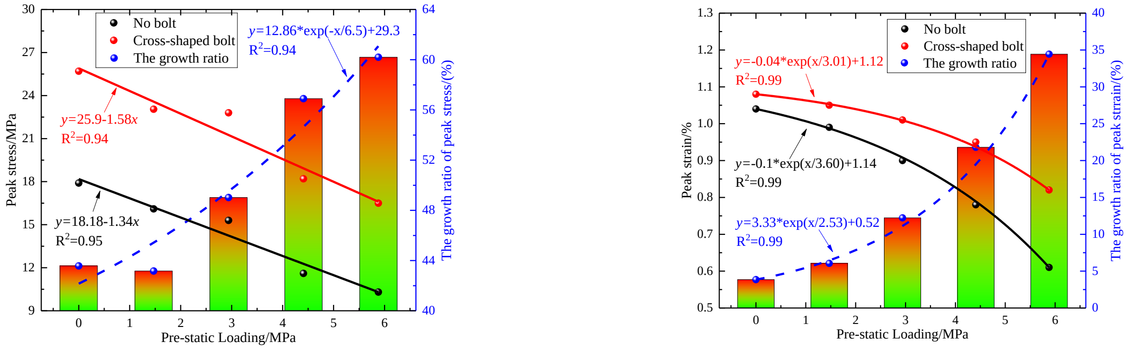

(a) (b)

Fig. 11 The dynamic mechanical parameters of two types of specimens under different pre-static load levels

rockbolt specimens are higher than those of the no-bolt specimen. Through fitting, the relationship between the strength and ultimate strain of the two types of specimens and the pre-static load level is obtained as follows

$$\sigma_n = 18.18 - 0.95P \quad R^2 = 0.95 \tag{12}$$

$$\sigma_a = 25.9 - 1.58P \quad R^2 = 0.94 \tag{13}$$

$$\varepsilon_n = -0.1e^{-\frac{P}{3.60}} + 1.14 \quad R^2 = 0.99 \tag{14}$$

$$\varepsilon_a = -0.04e^{-\frac{P}{3.01}} + 1.12 \quad R^2 = 0.99 \tag{15}$$

where σ_a is the strength of the rockbolt specimen; σ_n is the strength of the no-bolt specimen; ε_a is the ultimate strain of the rockbolt specimen; and ε_n is the ultimate strain of the no-bolt specimen.

To quantify the improvement of the dynamic mechanical properties of the rockbolt specimens, a strength improvement index and an ultimate strain improvement index are proposed in this paper. The strength improvement index and ultimate strain improvement index of the rockbolt specimen under static-dynamic coupled loading are as follows

$$\alpha = \frac{\sigma_a - \sigma_n}{\sigma_n} \tag{16}$$

$$\beta = \frac{\varepsilon_a - \varepsilon_n}{\varepsilon_n} \tag{17}$$

In Fig. 11, the vertical axis on the right side shows the rule of the strength improvement index and ultimate strain improvement index of the rockbolt specimen. Through fitting, it can be seen that the strength improvement index and ultimate strain improvement index of the rockbolt specimen increase with the pre-static load level, and the relationship between them is as follows

$$\alpha = 12.86e^{-\frac{P}{6.5}} + 29.3 \quad \mathrm{R}^2 = 0.94 \tag{18}$$

$$\beta = 3.33e^{-\frac{P}{2.53}} + 0.52 \quad \mathrm{R}^2 = 0.99 \tag{19}$$

3.4 Energy distribution in specimens dynamic fragmentation

3.4.1 Energy dissipation

According to formulas (5)-(7), the strain-time curve at the critical impact velocity is integrated, and the incident energy E_I, reflected energy E_R and transmitted energy E_T of the stress wave passing through the rockbolt specimen are obtained. The dissipated energy E_D of the specimen is obtained according to formula (8). The energy transfer characteristics of the specimen under different loading modes are shown in Fig 12. Considering that the striker velocity is controlled by air pressure and cannot be guaranteed to be equal, the ratio method was used to analyze the results. The ratio of reflection energy, transmission energy and dissipated energy to total input energy is expressed by $E_\mathrm{R}/E_\mathrm{I}$, $E_\mathrm{T}/E_\mathrm{I}$ and $E_\mathrm{D}/E_\mathrm{I}$, respectively. The statistical results are shown in Fig. 12.

According to Fig. 12, the following rules can be determined.

(a) Maximum incident energy: With the increase in the pre-static load level, the maximum incident energy of the two types of specimens decreases gradually, which is similar to the relationship between the critical strain rate and the pre-static load level in the above experimental results, indicating that the pre-static load level reduces the ability of the specimens to resist dynamic load impact.

(b) The ratio of dissipated energy: Both the dissipative energy E_D and the ratio of dissipative energy $E_\mathrm{D}/E_\mathrm{I}$ decreases with increasing pre-load level, and the ratio of dissipative energy decreases exponentially. The analysis shows that the pre-static load makes the specimen fit more closely with the bar, and it is easier for the incident wave to pass through the specimen to the transmission bar, increasing the ratio of transmission energy E_T. In the later stage of static-dynamic coupled loading, the specimen is destroyed, the incident wave cannot transmit to the transmission bar through the specimen, and the reflection wave is formed at the end face of the incident bar and the specimen. The larger the pre-static load level is, the larger

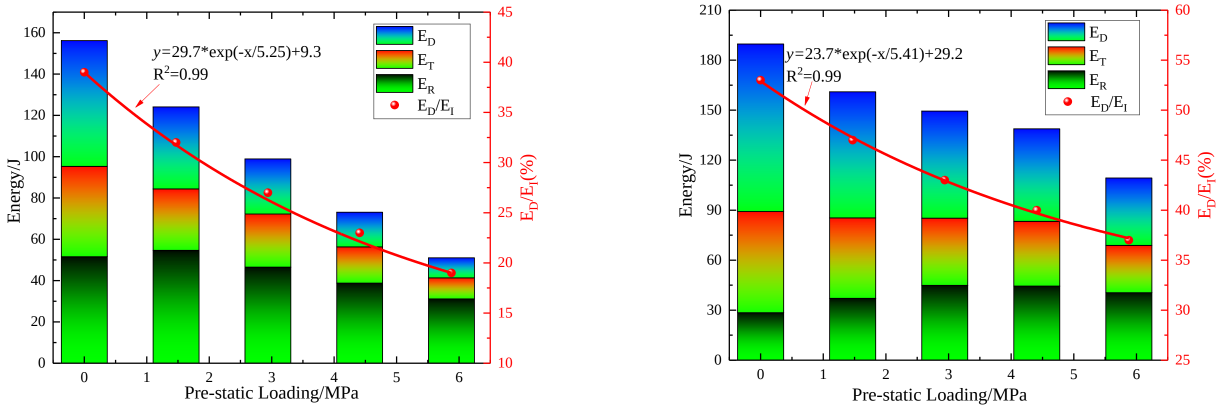

(a) No-bolt specimen (b) Rockbolt specimen

Fig. 12 Energy distribution in specimen dynamic fragmentation

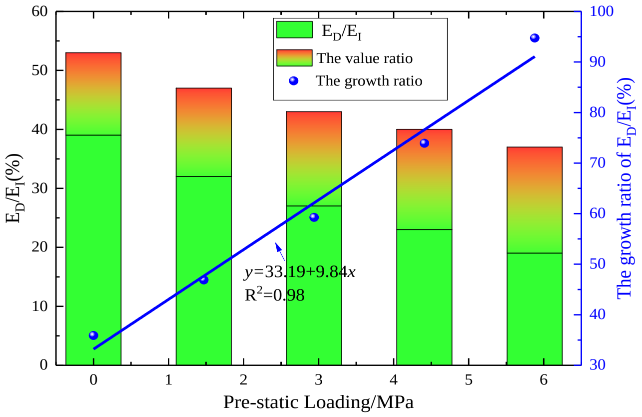

Fig. 13 Increase index of energy dissipation ratio of rockbolt specimen

the ratio of reflected energy is.

(c) Energy dissipation of the bolted rock mass: Compared with the energy distribution characteristics of the no-bolt specimen under static-dynamic coupled loading, it can be seen that the maximum incident energy and the dissipative energy of the bolted rock mass increased by 33 ~ 66 J and 30 ~ 40 J, respectively. Therefore, the ability to resist the dynamic load disturbance of a rock mass affected by high static load is improved after bolting.

3.4.2 Increase index of energy dissipation ratio

The characteristics of the dissipated energy show that the ratio of dissipated energy can represent an ability to resist impact. To quantify the improvement of the effect of the rockbolt on the impact resistance, an increase index of the dissipative energy ratio is proposed in this paper. The relationship between the increase index of the dissipative energy ratio and the pre-static load is as follows

$$\eta = \frac{\mu_a - \mu_n}{\mu_n} \tag{20}$$

where ψ_a is the E_D/E_I of the rockbolt specimen and ψ_n is the E_D/E_I of the no-bolt specimen.

As shown in Fig. 13, the increase index of the dissipation energy ratio of the rockbolt specimen is positively related to the pre-static load. When the pre-static load level is zero, the dissipation energy ratio of the rockbolt specimen is 53.0%, which is 35.9% higher than that of the no-bolt specimen; when the pre-static load level is 5.88 MPa, the dissipation energy ratio of the rockbolt specimen is 37.0%, and the increase index of energy dissipation ratio reaches 94.7%. The linear relationship between the increase index of the energy dissipation ratio and the level of the pre-static load is obtained by fitting.

$$\psi = 33.19 + 9.84p \quad R^2 = 0.98 \tag{21}$$

4 Guiding significance of anchoring support for deep underground roadway

The structure of the roof bolt is an important barrier in avoiding rockburst disasters in coal mines and plays an important role in preventing the occurrence of rockbursts. A rockburst occurs when the supporting roadway instantaneously fails under static-dynamic coupled loading, resulting in a severe throw-out of deep coal and rock. (Frid 2001, Hosseini 2017) The dynamic damage of the bolt structure in a coal roadway is caused by coupling additional dynamic effects on the basis of static action, which can be considered the result of the combined action of dynamic

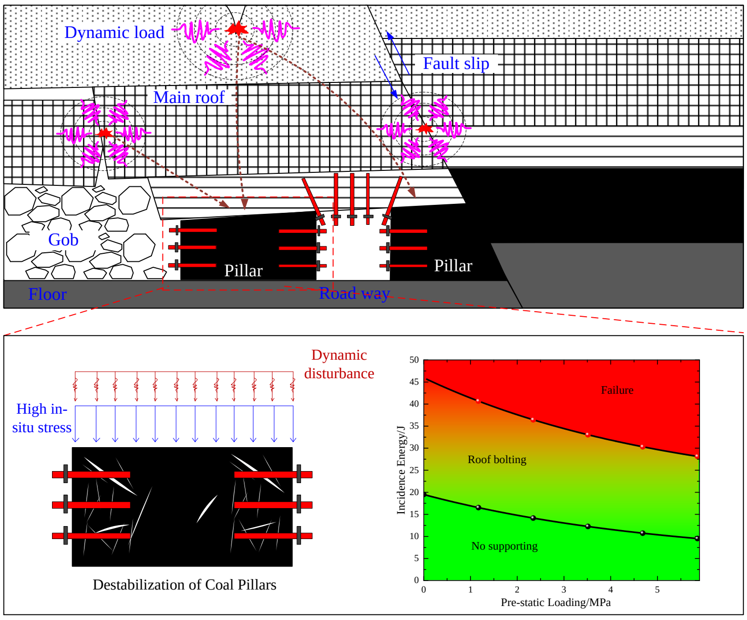

Fig. 14 Schematic diagram of surrounding rock under static-dynamic coupled loading

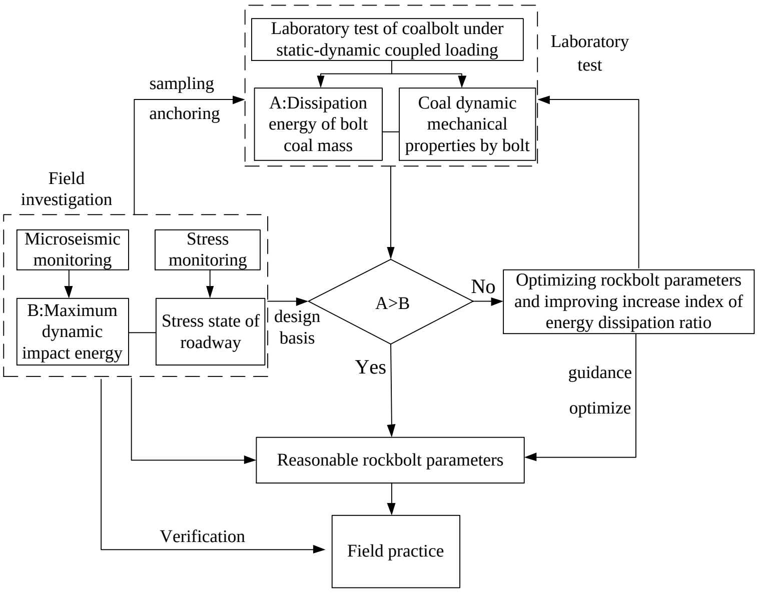

Fig. 15 Flow chart of bolt support design resistance to dynamic loading

and static loads (as shown in Fig. 14). The results show that ultimate strain rate, ultimate strength, ultimate strain and ultimate dissipation energy exist under different static-dynamic coupled loadings. This means that the surrounding rock of a deep roadway under a high static load will remain stable when the dynamic load disturbance is lower than the dynamic strain rate limit; otherwise, the roadway would be damaged. Bolt support can significantly improve the ultimate strain rate, ultimate strength, ultimate strain and ultimate dissipation energy of coal and rock mass and improve the ability of a deep roadway in surrounding rock to resist a dynamic impact.

The monitoring and early warning of rockbursts is based on the strength and energy conditions of rockbursts. At present, the rockburst prediction methods both home and abroad are mainly divided into three categories: the rock mechanics method (e.g., drilling cuttings), earth physics method (sound and microseismic monitoring), and experience analogy method. Among them, microseismic monitoring can monitor the fracture instability of the entire coal and rock mass and is widely used in deep coal mining in China. One of the main characteristics of the microseismic monitoring method is that it can accurately obtain the dynamic load energy value generated by an overburden fracture or fault slip in a deep stope. Combined with the research results, we put forward a roadway bolt support design method that is resistant to dynamic load disturbance, which can provide guidance for the design of deep underground roadway anchor supports. The specific process is shown in Fig. 15, and the details are as follows

(a). Field investigation: Combined with microseismic and stress monitoring, the maximum dynamic impact energy and stress distribution characteristics of the surrounding rock are obtained.

(b). Laboratory test: The ultimate dissipated energy and dynamic mechanics characteristics of coalbolt specimens are obtained under static-dynamic coupled loading.

(c). Bolt support design: Compare the maximum dissipation energy of the coalbolt specimen obtained in the laboratory with the maximum dynamic load impact energy of the mine determined by microseismic monitoring. If the dissipation energy obtained by the laboratory tests is greater than the maximum dynamic impact energy obtained by microseismic monitoring, then the roadway bolt support parameters are designed according to laboratory tests; otherwise, the bolt support parameters are redesigned.

(d). Verification: To ensure the practicality of bolt support parameters in the field roadway, monitor the stress state and deformation of the surrounding area, verify the rationality of bolt support parameters, and ensure the safety and stability of the roadway.

5. Conclusions

- The rebound characteristics of the bolted rock mass still exist after the peak of the stress-strain curve. In the later stage of dynamic impact, the rockbolt restrains the continuous development of the internal crack of the rockbolt specimens.
- The rock mass has a critical strain rate under different pre-static loadings. This means that the surrounding rock in a deep roadway under a high static load will remain stable when the dynamic load disturbance is lower than the dynamic strain rate limit; otherwise, the roadway will be damaged.
- The pre-static load reduces the ability of the rock mass to resist the impact of the dynamic load. The ratio E_D/E_I of dissipated energy of the rock mass decreases exponentially with increasing pre-static load. After bolting, the increasing index of the dissipation energy ratio to the bolted rock mass is positively correlated with the pre-static load.
- Based on laboratory testing and on-site microseismic and stress monitoring, this paper presents a design method for a roadway bolt support against dynamic load disturbance, which provides guidance for the design of deep underground roadway bolt supports and ensures the safety and stability of roadways threatened by impact.

Acknowledgments

The research described in this paper was financially supported by National Key R&D Program of China (no. 2018YFC0604703); National Natural Science Foundation of China (no. 52074170, 52074166, 51904163); Youth Foundation of Natural Science Foundation of Shandong Province (no. ZR2019QEE002, ZR2017BEE013). The authors express sincere thanks to the reviewers for their helpful comments and suggestions for improving this paper.

Conflicts of Interest

The authors declare no conflict of interest.

References

Ai, D., Zhao, Y., Wang, Q. and Li, C. (2019), "Experimental and numerical investigation of crack propagation and dynamic properties of rock in SHPB indirect tension test", *Int. J. Impact En.*, **126**, 135-146. https://doi.org/10.1016/j.ijimpeng.2019.01.001.

Ali, M. and Fatemeh, T. (2013), "A numerical study of the behavior of fully grouted rockbolts under dynamic loading", *Soil Dyn. Earthq. Eng.*, **54,** 66-72. https://doi.org/10.1016/j.soildyn.2013.08.003.

Aydan, Ö. (2019), "Dynamic response of support systems during excavation of underground openings", *J. Rock Mech. Geotech.*, **11**, 954-964. https://doi.org/10.1016/j.jrmge.2019.06.002.

Chang, X., Li, Z., Wang, S., Wang, S., Fu, L. and Tang, C. (2018), Pullout performances of grouted rockbolt systems with bond defects", *Rock Mech. Rock Eng.*, **51,** 861-871. https://doi.org/10.1007/s00603-017-1373-1.

Chang, X., Wang, G., Liang, Z., Yang, J. and Tang, C. (2017), "Study on grout cracking and interface debonding of rockbolt grouted system", *Constr. Build. Mater.*, **135**, 665-673. https://doi.org/10.1016/j.conbuildmat.2017.01.031.

Chen, F., Tang, C., Sun, X., Ma, T. and Du, Y. (2019), "Supporting characteristics analysis of constant resistance bolts under coupled static-dynamic loading", *J. Mountain Sci.*, **16**(5), 1160-1169. https://doi.org/ CNKI:SUN:SDKB.0.2019-05-015.

Du, H., Dai, F., Xu, Y., Liu, Y., Xu, Y., Liu, Y. and Xu, H. (2018), "Numerical investigation on the dynamic strength and failure behavior of rocks under hydrostatic confinement in SHPB testing", *Int. J. Rock Mech. Min. Sci.*, **108**, 43-57. https://doi.org/10.1016/j.ijrmms.2018.05.008.

Eremenko, A., Mashukov, I. and Eremenko, V. (2017), "Geodynamic and seismic events under rockburst-hazardous block caving in Gornaya Shoria", *J. Min. Sci.*, **53**(1), 65-70. https://doi.org/10.1134/s1062739117011859.

Faham, T., Zhang, C., Ismet, C., Onur, V. and Serkan, S. (2018), "Numerical and analytical simulation of the structural behaviour of fully grouted cable bolts under impulsive loading", *Int. J. Min. Sci. Technol.*, **28**, 807-811. https://doi.org/10.1016/j.ijmst.2018.08.012.

Feng, J., Wang, E., Chen, X. and Ding, H. (2018), "Energy dissipation rate: An indicator of coal deformation and failure under static and dynamic compressive loads", *Int. J. Min. Sci. Technol.*, **28**(3), 397-406. https://doi.org/10.1016/j.ijmst.2017.11.006.

Field, J., Walley, S., Proud, W., Goldrein, H. and Siviour, C. (2004), "Review of experimental techniques for high rate deformation and shock studies", *Int. J. Impact Eng.*, **30**(7), 725-775. https://doi.org/10.1016/s0734-743x(04)00052-1.

Freeman, T.J. (1978), "The behavior of fully bonded rock bolts in the kielder experimental tunnel", *Tunn. Tunnelling*, **10**(5), 37-40. https://doi.org/10.1016/0148-9062(78)91073-2.

Frid, V. (2001), "Calculation of electromagnetic radiation criterion for rockburst hazard forecast in coal mines", *Pure Appl. Geophys.*, **158**(5), 931-944. https://doi.org/10.1007/pl00001214.

Fu, Y., Sun, Z. and Ju, W. (2019), "Experimental study on static and dynamic mechanical properties of bolting wire mesh in rock burst roadway", *J. China Coal Soc.*, **44**(7), 2020-2029. https://doi.org/10.13225/j.cnki.jccs.2018.1392.

Gracaecosta, R., Alfaiate, J., Diasdacosta, D., Neto, P. and Sluys, J. (2013), "Generalisation of non-iterative methods for the modelling of structures under non-proportional loading", *Int. J. Fracture*, **182**(1), 21-38. https://doi.org/10.1007/s10704-013-9851-2.

He, M., Ren, F. and Liu, D. (2018), "Rockburst mechanism research and its control", *Int. J. Min. Sci. Technol.*, **28**, 829-837. https://doi.org/10.1016/j.ijmst.2018.09.002.

Hosseini, N. (2017), "Evaluation of the rockburst potential in longwall coal mining using passive seismic velocity tomography and image subtraction technique", *J. Seismology*, **21**(5), 1101-1110. https://doi.org/10.1007/s10950-017-9654-4.

Kang, H., Yang, J., Gao, F. and Li, J. (2020). "Experimental study on the mechanical behavior of rock bolts subjected to complex static and dynamic loads", *Rock Mech. Rock Eng.*, **53**(11), 4993-5004. https://doi.org/10.1007/s00603-020-02205-0.

Kozyrev, A., Panin, V., Semenova, I. and Zhuravleva, O. (2018), "Geodynamic safety of mining operations under rockburst-hazardous conditions in the Khibiny apatite eeposits", *J. Min. Sci.*, **54**(5), 734-743. https://doi.org/10.15372/ftprpi20180504.

Ning, J., Qiu, P., Yang, S., Shen, Z., Li, Z. and Wang, J. (2020), "Damage mechanism and support of surrounding rock anchorage structure of deep large section chamber under static-dynamic coupling loading", *J. Min. Saf. Eng.*, **37**(1), 50-61. https://doi.org/10.13545/j.cnki.jmse.2020.01.006.

Ning, J., Wang, J., Tan, Y. and Xu, Q. (2020), "Mechanical mechanism of overlying strata breaking and development of fractured zone during close-distance coal seam group mining", *Int. J. Min. Sci. Technol.*, **30**(2), 207-215. https://doi.org/CNKI:SUN:ZHKD.0.2020-02-008.

Peng, K., Liu, Z., Zou, Q., Zhang, Z. and Zhou, J. (2019), "Static and dynamic mechanical properties of granite from various burial depths", *Rock Mech. Rock Eng.*, **52**(10), 3345-3566. https://doi.org/10.1007/s00603-019-01810-y.

Sabetamal, H., Nazem, M., Carter, J. and Sloan, S. (2014), "Large deformation dynamic analysis of saturated porous media with applications to penetration problems", *Comput. Geotech.*, **55**, 117-131. https://doi.org/10.1016/j.compgeo.2013.08.005.

Vandermaat, D., Saydam, S., Hagan, P. and Crosky, A. (2016), "Examination of rockbolt stress corrosion cracking utilising full size rockbolts in a controlled mine environment", *Int. J. Rock Mech Min. Sci.*, **81**, 86-95. https://doi.org/10.1016/j.ijrmms.2015.11.007.

Wang, A., Gao, Q., Dai, L., Pan, Y., Zhang, J. and Chen, J. (2018), "Static and dynamic performance of rebar bolts and its adaptability under impact loading", *J. China Coal Soc.*, **43**(11), 2999-3006. https://doi.org/10.13225/j.cnki.jccs.2018.8020.

Wang, B., Li, X., Ma, C. and Fan, B. (2014), "Principle and preliminary application of combined static-dynamic support to rockburst disaster controlling", *Chinese J. Rock Mech. Eng.*, **33**(6), 1169-1178. https://doi.org/CNKI:SUN:YSLX.0.2014-06-010.

Wang, W., Song, Q., Xu, C. and Gong, H. (2018), "Mechanical behaviour of fully grouted GFRP rock bolts under the joint action of pre-tension load and blast dynamic load", *Tunn. Undergr. Sp. Tech.*, **73**, 82-91. https://doi.org/10.1016/j.tust.2017.12.007.

Wu, Q., Chen, L., Shen, B., Dlamini, B., Li, S. and Zhu, Y. (2019a), "Experimental investigation on rockbolt performance under the tension load", *Rock Mech. Rock Eng.*, **52**, 4605-4618. https://doi.org/10.1007/s00603-019-01845-1.

Wu, Q., Zhao, F., Wang, S., Zhou, Z., Wang, B. and Li, Y. (2019b), "Mechanical response characteristics of full grouted rock boltssubjected to dynamic loading", *Rock Soil Mech.*, **40**(3), 942-950. https://doi.org/10.16285/j.rsm.2017.1831.

Wu, Y., Chen, J., Jiao, J., Zheng, Y. and He, J. (2018), "Damage and failure mechanism of anchored surrounding rock with impact loading", *J. China Coal Soc.*, **43**(9), 2389-2397. https://doi.org/10.13225/j.cnki.jccs.2018.0415.

Yu, S., Zhu, W., Niu, L., Zhou, S. and Kang, P. (2019), "Experimental and numerical analysis of fully grouted long rockbolt load-transfer behavior", *Tunn. Undergr. Sp. Tech.*, **85**, 56-66. https://doi.org/10.1016/j.tust.2018.12.001.

Zhu, W., Jing, H., Yang, L., Pan, B. and Su, H. (2018), "Strength and deformation behaviors of bedded rock mass under bolt reinforcement", *Int. J. Min. Sci. Technol.*, **28**(4), 593-599. https://doi.org/10.1016/j.ijmst.2018.03.006.

CC